Photoisomerization of a 4-dicyanomethylene-2-methyl-6-(p -dimethylaminostyryl)-4 H -pyran analog dye: a combined photophysical and theoretical investigation

Yang Zhou, Stéphane Maisonneuve, Lorenzo Casimiro, Pascal Retailleau, Juan Xie, François Maurel, Rémi Métivier

PCCP

ARTICLE TYPE

Cite this: DOI: 00.0000/xxxxxxxxxx

Photoisomerization of a 4-dicyanomethylene-2-methyl-6-(*p*-dimethylaminostyryl)-4*H*-pyran analog dye: a combined photophysical and theoretical investigation†

Yang Zhou,[a] Stéphane Maisonneuve,[a] Lorenzo Casimiro,[a] Pascal Retailleau,[b] Juan Xie,[a] François Maurel,*[c] and Rémi Métivier*[a]

Received Date
Accepted Date

DOI: 00.0000/xxxxxxxxxx

A combination of experimental and theoretical investigations of a photoisomerizable analog of 4-dicyanomethylene-2-methyl-6-(*p*-dimethylaminostyryl)-4*H*-pyran (DCM) dye molecule is presented. We provide evidences that the 4 main isomers and conformers of DCM contribute to its photochemical and photophysical processes. Absorption and emission spectra, as well as time-resolved fluorescence experimental results, are discussed and compared to DFT/TDDFT calculations. The *E*↔*Z* isomerization is induced photochemically, whereas the *s-cis*↔*s-trans* conformational interconversion is a thermal process which may also happen during irradiation. The photoreaction pathways from the first excited state down to the ground state is shown to be mediated by two conical intersections, as depicted by spin-flip TDDFT calculations. The rationalization of these isomerization schemes provides important insights into the photophysical properties of DCM, responsible for its photoswitchable fluorescence.

Introduction

Molecular photoswitchable systems consist of chromophores that can be interconverted by light stimuli between at least two states, resulting in different photochemical and photophysical properties. Light-induced reactions involve photoinduced electrocyclization, cycloreversion, dimerization, photoinduced bond cleavage, *E*↔*Z* or *cis*↔*trans* isomerization. Among these mechanisms, the double-bond *E*↔*Z* photoisomerization is prevailing in light-driven molecular switches, rotors and sensors due to its flexibility and embeddability.[1–4] The tunable optical and mechanical properties upon irradiation provided by the double-bond isomerization allow applications such as light-sensitive sensors and functional materials.[5–7] The N=N, C=N and C=C bonds are the most common photoswitchable groups in azobenzenes[8,9], acylhydrazones[10–12], and stilbenes[13], respectively.

Besides, 4-dicyanomethylene-2-methyl-6-(*p*-dimethylaminostyryl)-4*H*-pyran (DCM) analogs are well-known red-emitting dyes, used in lasers,[15–17] in capping layers of organic light emitting diodes (OLEDs) or in dye-sensitized solar cells (DSSCs).[18–22] Its donor-π-acceptor structure confers it a noticeable intermolecular charge transfer character and consequently, a strong solvatochromism. Because of its central C=C double-bond, DCM can undergo an *E*↔*Z* isomerization under irradiation. However, the photoisomerization properties of DCM have been ignored in the vast majority of reports, with a few notable exceptions.[14,23–29] The *E*↔*Z* photoisomerization studies and the related conversion yield quantification of a DCM analog (DCM-*o*-alkyne), have been reported by our group.[14] In this previous article, we described the steady-state spectroscopy, HPLC analysis, conversion yield and photostationary states (PSSs), characterization of the *E*-form and *Z*-form, under illumination, at different wavelengths and in different solvents.

Indeed, the *E*-forms of DCM-*o*-alkyne were found to be fluorescent, and not the *Z*-forms. Thus, the fluorescence modulation associated to the photoisomerization demonstrates the high potential of DCM analogs as intrinsic photoswitchable fluorophores. The previous studies on DCM, using spectroscopic or quantum chemical calculations, indicated the existence of 4 stable isomers (*E*- and *Z*-forms) and conformers (*s-cis*- and *s-trans*-forms) and their possible interconversions.[14,29]

[a] *Université Paris-Saclay, ENS Paris-Saclay, CNRS, Photophysique et Photochimie Supramoléculaires et Macromoléculaires, 91190 Gif-sur-Yvette, France. E-mail: remi.metivier@ens-paris-saclay.fr*

[b] *Université Paris-Saclay, CNRS, Institut de Chimie des Substances Naturelles, UPR 2301, Gif-sur-Yvette, France.*

[c] *Université de Paris, ITODYS, CNRS, F-75006 Paris, France. E-mail: maurel@univ-paris-diderot.fr*

† Electronic Supplementary Information (ESI) available: X-ray diffraction analyses, details of DFT/TDDFT and conical intersections calculations. See DOI: 10.1039/cXCP00000x/

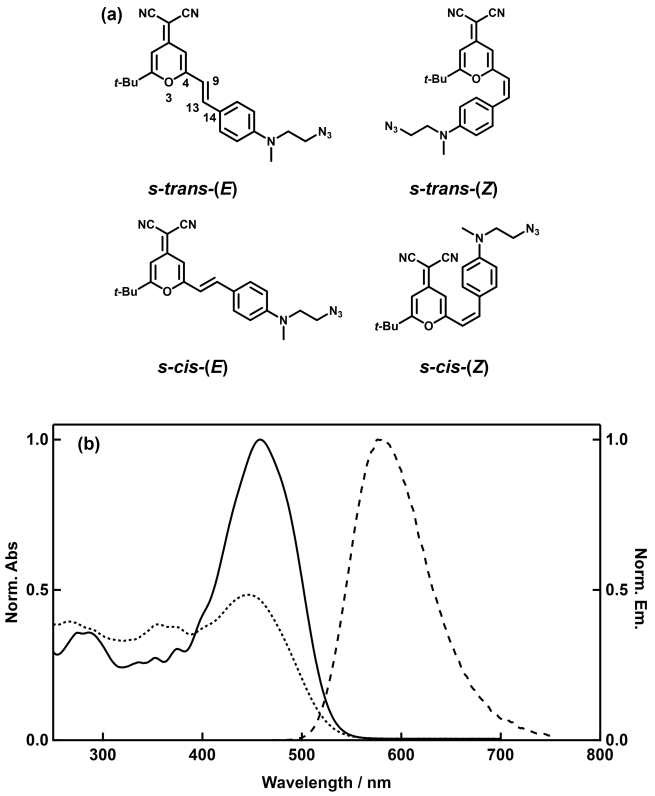

Fig. 1 (a) Molecular structures of DCM-azide in its different isomers and conformers, noted *s-trans*-(*E*), *s-cis*-(*E*), *s-trans*-(*Z*), *s-cis*-(*Z*) according to our previous study [14]. Dihedral ($O_3-C_4-C_9=C_{13}$) involving C-C single bond is defined as D1 and dihedral ($C_4-C_9=C_{13}-C_{14}$) involving C=C double bond is defined as D2. **(b)** Absorption spectra of the *E*-isomer (full line on the left) and the *Z*-isomer (dotted line on the left) together with *E*-isomer emission (dashed line on the right) are recorded in THF solution.

In the present paper, we focus our attention on the DCM-azide [30], an azido variant of the previously studied DCM-*o*-alkyne, allowing further functionalization. The molecular structures of the four isomers/conformers of DCM-azide are shown in Figure 1. Like other molecular systems with asymmetric stilbene core, the detailed description of the behavior of DCM-azide under illumination in its different isomers/conformers is not straightforward, and the interconversion modes between the four geometries are still not clearly understood. In this context, the combination of spectroscopic and computational approaches can be helpful to rationalize the DCM-azide properties. We report here the experimental and theoretical studies of DCM-azide involving its four forms, to bring in-depth description of its photophysical and photochemical properties. X-ray structures, steady-state and time-resolved spectroscopy data, as well as quantum chemical computations in the ground state, the excited state, or at conical intersections, provide important information on the photoisomerization pattern of DCM-azide.

Results and discussion

Structural studies

The DCM-azide has been synthesized as pure *E*-form according to the previously reported procedures [30] by shielding the reaction and post-procedures from ambient UV-visible light exposures. By the different eluent conditions on the column chromatographies, the DCM-azide can be obtained as a red crystalline powder. In the following, we denote two key dihedral angles, $O_3-C_4-C_9=C_{13}$ and $C_4-C_9=C_{13}-C_{14}$ of the molecular layout in Figure 1, as D1 and D2, respectively.

After recrystallizing the crystalline powder, two different polymorphs were obtained as single crystals. The corresponding structures were successfully solved by X-ray diffraction (XRD) analyses, as shown in Figure 2 and in the ESI (Figure S1 and Table S1): the first one crystallizes in the triclinic *P*-1 space group, whereas the second one adopts an orthorhombic *P*nma space group. The molecular packing mainly influences the orientation of the azido substituent, while the whole structure is in both cases thoroughly planar across the central double-bond of DCM-azide, shown in the *s-trans*-(*E*) configuration, for both structures (see ESI, Figure S2). The two polymorphs differ mainly in the intermolecular contacts, as shown by Hirshfeld surface analyses described in ESI (Figures S3-S5). The molecular geometry of DCM-azide is defined by the two main dihedral angles D1 and D2 (D1 = 4.7° and D2 = 179.9° for the triclinic form, and D1 = 0.0° and D2 = 180.0° for the orthorhombic form), and the corresponding C_4-C_9 single-bond (length = 1.440 Å and 1.434 Å for triclinic and orthorhombic forms, respectively) and $C_9=C_{13}$ doube-bond (length = 1.335 Å and 1.340 Å for triclinic and orthorhombic forms, respectively). These geometrical parameters are fully in line with the previously described DCM-*o*-alkyne derivative. [14]

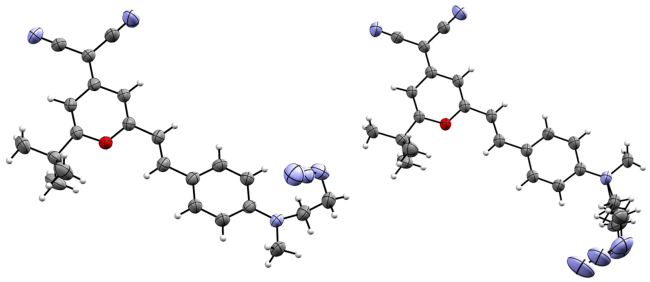

Fig. 2 X-ray diffraction structures in the triclinic form (left) and in the orthorhombic form (right) of the *s-trans*-(*E*) form of DCM-azide obtained after crystallization.

In the previous study on DCM-*o*-alkyne, the THF solvent (medium polarity) was revealed to be an ideal trade-off between the fluorescence quantum yield and the $E\rightarrow Z$ photoisomerization conversion yield, outperforming acetonitrile and toluene in terms of fluorescence photoswitching benchmark. Therefore, we decided to employ THF as the main solvent in the present study of DCM-azide. In the steady-state UV-visible measurements, DCM-azide shows an absorption λ_{max} at 459 nm in THFm, with a molar absorption coefficient recorded at $\varepsilon_{459\ nm}$ = 48700 $Lmol^{-1}cm^{-1}$.

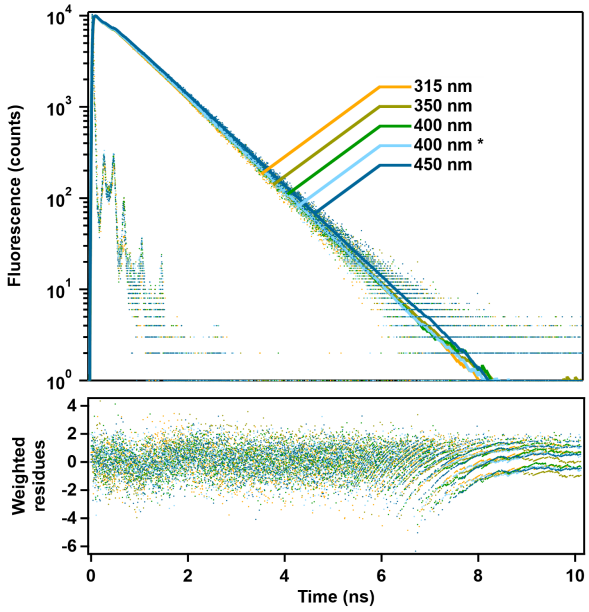

Fig. 3 Fluorescence decay curves, instrumental response function, bi-exponential fitting and weighted residuals of DCM-azide at different excitation wavelengths (315 nm, 350 nm, 400 nm and 450 nm) in THF. The marked decay (*) corresponds to a DCM-azide THF solution irradiated at 485 nm.

After reaching a photostationary state under irradiation at 485 nm (PSS485), the λ_{max} was shortened and the absorption bands around 350 - 450 nm were flattened. Furthermore, from the PSS485 solution, we extracted the *Z*-form of DCM-azide by thin layer chromatography (TLC), and measured its absorption spectrum in THF. The corresponding dotted absorption spectrum shown in Figure 1 presents a much weaker and blue-shifted band at 447 nm, and the absorption is stronger in the 300-400 nm range than the synthesized *E*-form.

The fluorescence spectrum of DCM-azide in the *E*-form is broad and intense around 590 nm, and its emission quantum yield is appreciable ($\Phi_f = 0.25$) but lower than that of DCM-*o*-alkyne ($\Phi_f = 0.32$),[14] due to its azido lateral part. Fluorescence decay curves of DCM-azide were recorded at different excitation wavelengths by the time-correlated single-photon counting (TCSPC) technique (Figure 3). The fluorescence decays were fitted by a global analysis procedure using a bi-exponential function, which was necessary to obtain acceptable curve fitting ($\chi^2_R < 1.2$). Two decay-times were identified: the first decay-component (τ_1) is found at 0.84 ns contributing to the major part of the fluorescence (large pre-exponential factor $\alpha_1 > 0.88$ and fraction of intensity $f_1 > 0.97$), whereas the second decay-time is shorter ($\tau_2 = 0.20$ ns) and has a minor contribution to the fluorescence intensity ($\alpha_2 < 0.12$ and $f_2 < 0.03$). We collected the fluorescence decays at different excitation wavelengths from 315 nm to 450 nm and irradiated the DCM-azide sample at 485 nm to make cross comparisons, and further evaluate the possible contributions of the *Z*-isomer to the emission. As a result, the change of excitation wavelength or irradiation did not influence the collected fluorescence decays: τ_1 and τ_2 were found to be identical, and $\alpha_1 = 0.91 \pm 0.03$, $\alpha_2 = 0.09 \pm 0.03$ were similar for all the measurements, as shown in Figure 3 and Table 1. Therefore, the two decay-time components are not related to the $E \leftrightarrow Z$ photoisomerization process. The results from Table 1 fully confirm the interpretation reported in our previous paper.[14] From fluorescence decays collected at different excitation wavelengths, with or without irradiation, we can conclude that the *Z*-forms of DCM-azide are completely non-emissive, and the fluorescence components (τ_1 and τ_2) identified by fluorescence decays correspond to *s-trans*-(*E*) and *s-cis*-(*E*) conformers.

Table 1 Time-resolved fluorescence parameters of DCM-azide in the *E*-form, determined in THF.

λ_{ex}(nm)	τ_1 (ns)	$\alpha_1(f_1)$	τ_2 (ns)	$\alpha_2(f_2)$
315	0.84	0.89(0.97)	0.20	0.11(0.03)
350	0.84	0.93(0.98)	0.20	0.07(0.02)
400	0.84	0.88(0.97)	0.20	0.12(0.03)
400*	0.84	0.89(0.97)	0.20	0.11(0.03)
450	0.86	0.92(0.98)	0.17	0.08(0.02)

*: after irradiation to at 485 nm (PSS485)

Table 2 Absorption and emission transition energies of *s-trans*-(*E*) form DCM-azide, calculated by TDDFT with the 6-311G++(d,p) basis set in THF, together with experimental data recorded for the *E*-form in THF solution.

	PBE0		CAM-B3LYP		ωB97X-D		Exp. data	
	(eV)	(nm)	(eV)	(nm)	(eV)	(nm)	(eV)	(nm)
λ_{abs}	2.68	463	3.06	405	3.15	394	2.70	459
λ_{em}	2.38	521	2.44	509	2.45	507	2.15	576
Stokes shift	2404 cm^{-1}		5045 cm^{-1}		5657 cm^{-1}		4425 cm^{-1}	

Absorption and emission electronic transitions of *s-trans*-(*E*) isomer

From the X-ray structure of DCM-azide, we assume that the *s-trans*-(*E*) isomer corresponds to its most stable isomer. Moreover, the steady-state and time-resolved fluorescence results demonstrated that the *s-trans-(E)* isomer is considered to represent the main contribution to the fluorescence. Therefore, absorption and emission energy calculations at the level of density functional theory (DFT) and time-dependent density functional theory (TDDFT) were first performed for this isomer. Computations with polarizable continuum model (PCM) for THF, three functionals (PBE0, CAM-B3LYP, ωB97X-D), and the 6-311+G(d,p) Pople basis set were performed for DCM-azide in the *s-trans-(E)* form. All electronic transition energies were calculated by the linear-response method. Other non-equilibrium solvation calculations were also tested, as reported in the ESI (corrected linear-response and state-specific, see Table S6).

By screening the DFT functionals, PBE0 shows the most accurate estimation of the DCM-azide absorption (λ_{abs}= 463 nm, compared to the experimental value λ_{max} = 459 nm) and at the same time rather acceptable emission estimation compared to the experiment (λ_{em} = 521 nm vs. experimental λ_{max} = 576 nm). Despite the donor-acceptor character of DCM-azide, ωB97X-D and CAM-B3LYP did not provide better absorption or emission energies compared to PBE0, with systematic overestimation of transition energies and shorter maximum wavelengths than those measured experimentally. Only the Stokes shift is more accurately described with the long-range corrected CAM-B3LYP. Considering

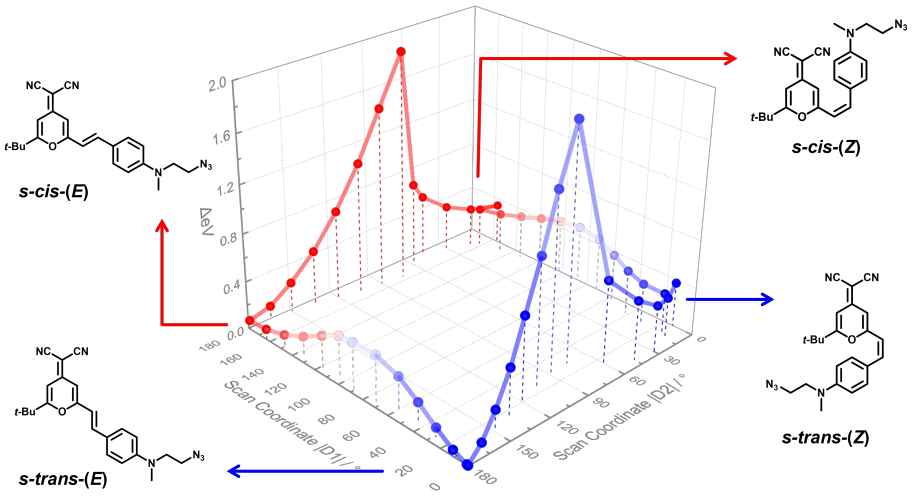

Fig. 4 The S_0 Potential energy curves of the DCM-azide isomers/conformers interconversion by rotating the main dihedral angles D1 and D2, D1 corresponding to the $O_3-C_4-C_9=C_{13}$ scan coordinate and D2 corresponding to the $C_4-C_9=C_{13}-C_{14}$ scan coordinate (See Figure 1). DFT calculations were performed at the PBE0/6-311+G(d,p) PCM:THF level of theory. The calculated scans were performed along the following coordinate directions: *s-cis*-(*E*)→*s-cis*-(*Z*), *s-cis*-(*E*)→*s-trans*-(*E*), *s-trans*-(*E*)→*s-trans*-(*Z*) and *s-cis*-(*Z*)→*s-trans*-(*Z*). The *s-cis* side is shown in red color and the *s-trans* side is shown in blue color. NB: the final states reached in the end of scans may slightly differ from the fully optimized forms (as visible *e.g.* for *s-cis*-(*Z*) and *s-trans*-(*Z*))

all the functional screenings and computational costs, we decided to select PBE0 as the main functional for the DFT studies, for more intuitive comparisons and uniformity over the whole theoretical investigation (see "Excited state computations" paragraph below).

We analyzed the frontier molecular orbitals of the four isomers/conformers of DCM-azide at PBE0/6-311G++(d,p) level with PCM model of THF solvent, as reported in the ESI (Figure S6). For all forms, the highest occupied molecular orbitals (HOMOs) and the lowest unoccupied molecular orbitals (LUMOs) are the main orbitals involved in the first electronic transition $S_0 \rightarrow S_1$. The HOMOs (respectively LUMOs) have a clear π (respectively π^*) character. Therefore, the $S_0 \rightarrow S_1$ transition has a $\pi \rightarrow \pi^*$ nature, with a limited charge-transfer character due to a small electronic delocalization from the methylamino-styryl moiety to the dicyano-pyran moiety. Multiple contributions of the HOMO-1, HOMO, LUMO and LUMO+1 to the $S_0 \rightarrow S_2$ and $S_0 \rightarrow S_3$ electronic transitions are noted. In a similar manner, such features were also identified for the other functionals tested, namely ωB97X-D and CAM-B3LYP, and other polar solvents (see ESI, Figures S7-S10).

Ground-state potential energy surface

As previously described, the four stable forms of DCM derivatives are denoted as *s-trans*-(*E*), *s-cis*-(*E*), *s-trans*-(*Z*), *s-cis*-(*Z*). Their corresponding ground state geometries and energies were optimized at the DFT PBE0/6-311G++(d,p) level (ESI, Tables S2-S5). *s-trans*-(*E*) shows the lowest energy, which confirms the X-ray structure analysis. Both *E*-forms have straight planar geometries across the double-bond moiety. Within a PCM model of THF solvent, the dipole moment of *s-trans*-(*E*) records the highest value at 20.0 D, while *s-cis*-(*Z*) has the lowest dipole moment 12.8 D amongst the four (ESI, Figures S6). The dipole moments were enhanced in more polar solvents such as acetonitrile and DMSO (see ESI, Figures S9-S10) with more stabilized energies.

The ground-state pathway of the interconversion between the *s-trans* and *s-cis* conformers can be followed by rotating the C_4-C_9 single-bond, thus changing the D1 dihedral angle, the *E*-isomer being transformed into its corresponding *Z*-isomer by changing the D2 dihedral angle (rotation around the $C_9=C_{13}$ double bond). The scanning plot of these energy minimized paths along the two rotating dihedral angles D1 and D2 is presented in Figure 4. For the *s-cis*↔*s-trans* interconversion, the energy barriers are calculated to be 0.41 eV and 0.16 eV for the *E*-side and the *Z*-side, respectively. Regarding the $E \leftrightarrow Z$ reaction, the curves show that the closed-shell formalism cannot be used for double-bond rotation but clearly illustrate that the $E \leftrightarrow Z$ barrier of isomerization is much higher than the *s-cis*↔*s-trans* process, as expected. Therefore, the ground-state *s-cis*↔*s-trans* transformation can occur spontaneously at room temperature, whereas the $E \leftrightarrow Z$ requires external energy input to take place, such as photon absorption. The C_4-C_9 and $C_9=C_{13}$ bond lengths vs. scan coordinates D1 and D2 are shown in the ESI (Figure S11, blue and red lines, respectively), presented by the blue and red lines, respectively. Along the *s-cis*↔*s-trans* interconversion, the double bond remains almost unaffected, whereas the single bond is elongated to a maximum at the transition states, then shortened at the four stable isomers and conformers structures. Along the $E \leftrightarrow Z$ isomerization paths, the double bond is elongated and the single bond is shortened to reach comparable bond lengths at the transition states ($C_9=C_{13}$ max. = 1.419 Å, C_4-C_9 min. = 1.399 Å). When the molecule is distorted around D2 = 75°, the $C_4-C_9=C_{13}-C_{14}$ loses the alternate single-double-single bond character at this peculiar geometry. Indeed, the $E \leftrightarrow Z$ transformation is a configura-

tional isomerization, which requires that the double bond adopts a "single bond" character. In the present case, these elements lead us to assume that the $E \leftrightarrow Z$ photosiomerization is allowed in the excited state (see below).

Excited-state computations

The role of the dihedral angle D1 corresponding to the *s-cis*↔*s-trans* interconversion processes, was first investigated in the excited state. We performed the relaxed scan optimization of their lowest excited-state S_1 PECs with a downsized def2-SVP basis set, as well as the S_1 vertical excitation energies (VEEs), as shown in the ESI (Figure S12). By examining the *s-cis*↔*s-trans* excited-state interconversion, the optimized S_1 energy levels are only slightly lower than the S_1 VEEs *i.e.*, the lowest excited-state geometries are almost identical to the Frank-Condon ones. The scan optimizations of the S_1 states imply even higher energy barriers than the ground states for the two conformational interconversions: 0.70 eV in the S_1 vs. 0.44 eV in the S_0 (*s-cis*-(E)→*s-trans*-(E)) and 0.40 eV in the S_1 vs. 0.17 eV in the S_0 (*s-cis*-(Z)→*s-trans*-(Z)). On the other side, regarding the $E \leftrightarrow Z$ isomerization, TDDFT optimizations could not be performed due to the possible conical intersection (CI) encountered, which requires other multi-determinantal methods.

As an extension to explore the potential energy surface (PES) along the $E \leftrightarrow Z$ isomerization, we searched the possible existence of CIs on the reaction path by using the Spin-Flip TDDFT (SF-TDDFT) method.[31,32] SF-TDDFT is a single reference method, easy to carry out to compensate the inability of TDDFT to localize S_0/S_1 CIs.[33,34] Taking a higher triplet state with two unpaired $\alpha-$electrons as the reference state instead of the ground state used in TDDFT, SF-TDDFT is able to describe doubly-excited electron configurations *via* $\alpha \rightarrow \beta$ spin-flipped excitations necessary to calculate CIs where the Born-Oppenheimer approximation breaks down. However, we need to pay attention to the spin contamination problem brought by the single reference method. When applied to double-bond molecular systems, *e.g.* stilbene or azobenzene, the SF-TDDFT method with different algorithms has successfully yielded results close to the CASSCF/CASPT2 level of calculations at a rather lower computational cost.[33–35] In the present case, we adapted SF-TDDFT with the penalty constrained algorithm to DCM-azide, which is a 54-atom dimension system, searching the minimum energy CIs on the S_0/S_1 PES.[33]

To localize the CI, we firstly implemented a S_0 PES scan map with a reduced basis set size at 6-31G(d) *in vacuo*. The global S_0 PES is shown in Figure 5. Despite slight energy differences, the results are well-compatible with the larger basis set used with the PCM solvation model (Figure 3). Then we assumed the CIs to be located close to the maximum energy barrier between the *E*- and *Z*-forms. We defined a set of initial geometries corresponding to the S_0 PES map, with D2 = -75° and D1 ranging from -180° and +180°, sampling one structure every 15°. With this methodology, two CI(S_0/S_1) geometries were successfully identified as depicted in Figure 5 and detailed in ESI (Tables S7-S8), of the *s-cis* type (CI-1: D1 = 176.66°, D2 = -78.58°) and *s-trans* type (CI-2: D1 = 18.88°, D2 = -87.40°), respectively. At the first glance, the CIs are close to the location of the highest energy barrier structures of the S_0 PES. The *s-cis* CI-1 is geometrically close to the ground state geometry taken at the transition state between *s-cis*-(E) and *s-cis*-(Z) as shown in Figure 5. The CI-2 geometry found on the *s-trans* side is more displaced from the saddle point of the ground state between the *s-trans*-(E) and *s-trans*-(Z). However, the two CIs identified by SF-TDDFT have a similar S_0/S_1 energy at this calculation level (CI-1: S_0/S_1 = -1292.8950/-1292.8935 a.u. and CI-2: S_0/S_1 = -1292.8945/-1292.8935 a.u., respectively), with comparable single $C_4 - C_9$ and double $C_9 = C_{13}$ bond lengths (CI-1: 1.399/1.464 Å and CI-2: 1.395/1.456 Å, respectively). Both CI-1 and CI-2 most probably originate from the same seam of intersection between S_0 and S_1, along the D1 dihedral angle rotation. In addition, it is interesting to note that the electronic nature of the S_1 state at the crossing could be provided by the SF-TDDFT and was found to have an ionic HOMO→LUMO character.

Table 3 Energies and dihedral angles of optimized S_1 and CI, computed at the SF-PBE0/6-31G(d) level.

	ΔE of S_1 (eV)	D1 (°)	D2 (°)
S_1 of *s-trans*-(E)	-	0.12	179.41
S_1 of *s-cis*-(E)	0.058	-179.32	179.74
S_1 of *s-trans*-(Z)	0.290	4.66	18.63
S_1 of *s-cis*-(Z)	0.088	-171.35	23.92
CI-1 (*s-cis*)	0.512	171.66	-78.58
CI-2 (*s-trans*)	0.511	18.88	-87.40

Moreover, we computed the S_1 minima for the *s-trans*-(E), *s-cis*-(E), *s-trans*-(Z), *s-cis*-(Z) forms, at the SF-PBE0/6-31G(d) level in vacuum, to be compared with CI-1 and CI-2. Their relative energies and dihedral angles (D1 and D2), together with those of CI-1 and CI-2, are gathered in Table 3. The energy difference between the optimized S_1 state and the CI is higher for the *s-trans*-(E) form (ΔE = 0.51 eV). The lowest energy differences are obtained for the *Z*-forms (ΔE = 0.22-0.42 eV). The *s-cis*-(E) is located at an intermediate level (ΔE = 0.45 eV). Additionally, the optimized S_1 states for both *E*-forms show a fully planar geometry, whereas they appear more tilted for the *Z*-forms, with 5-9° away from planarity for D1, and 18-24° for D2. The geometries of the excited state of the *Z*-forms being closer to the CI ones, compared to the planar *E*-forms, we can therefore expect a much lower energy barrier in the excited state landscape to reach the CI after excitation and return non-radiatively to the ground state, possibly along with photoisomerization. Consequently, we can deduce that the DCM-azide molecule has several pathways to relax from the excited states to the ground state. When DCM-azide is excited, it can undergo an isomerization in the excited state, through the CI to reach the ground state, which is fully compatible with the experimental evidence of the $E \leftrightarrow Z$ photoisomerization. Besides, the relaxed excited states of DCM-azide can return to the ground state by radiative deactivation. Since the S_1 excited state of the *s-trans*-(E) form has a larger energy difference than the *s-cis*-(E) form to reach the CI, it could explain its much larger contribution to the overall emission and its longer lifetime. The S_1 excited states of the *Z*-forms being much closer to the CI (in geometry and energy), it is fully in line with the absence of observed fluorescence from

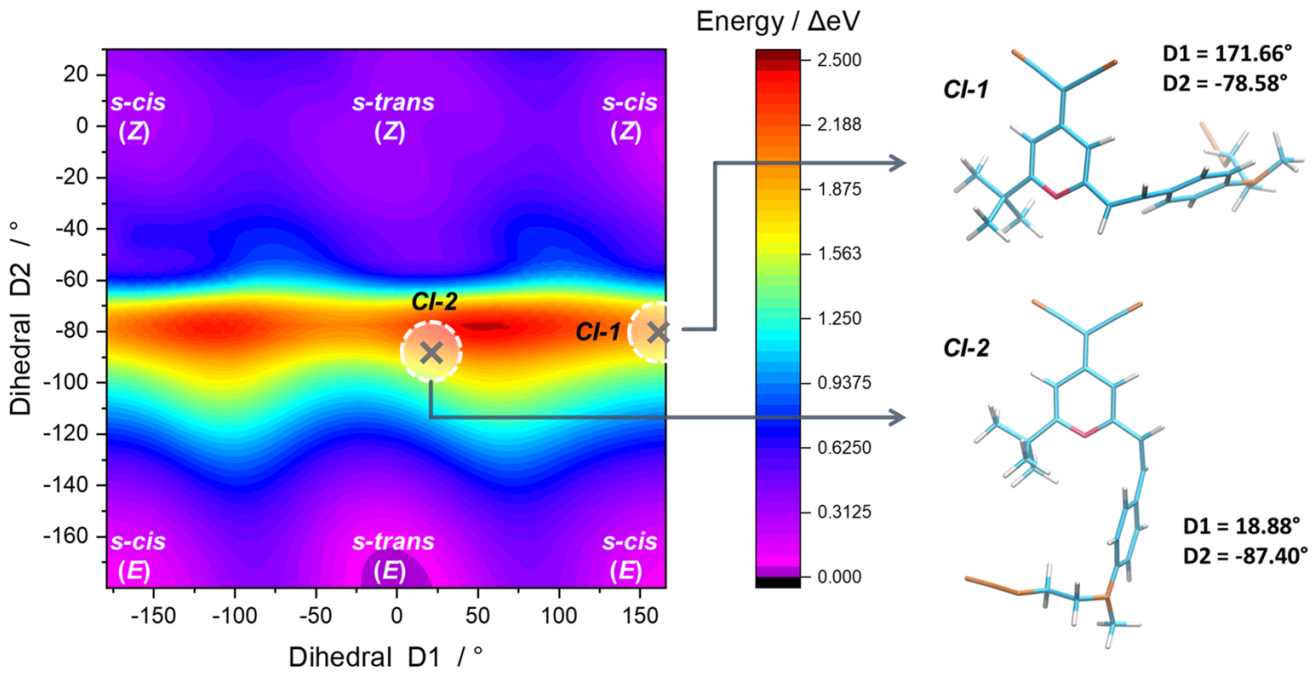

Fig. 5 Ground-state potential energy surface (PES) calculated by DFT (PBE0/6-31G(d)) *in vacuo* as a function of D1 and D2 dihedral angles (color map), and minimum energy conical intersection (CI) geometries localized in the S_0 PES map, calculated by the SF-TDDFT method at the PBE0/6-31G(d) *in vacuo* level of theory.

these species, as well as the higher photoisomerization quantum yield measured previously for the $Z \rightarrow E$ reaction, compared to the $E \rightarrow Z$ reaction.[14]

As a unified general picture, after light absorption, the *E*-forms may experience a competition between fluorescence deactivation, $E \rightarrow Z$ isomerization reaction (through CIs), and other non-radiative deactivation pathways. Regarding the *Z*-forms, which are not emissive, only the $Z \leftrightarrow E$ isomerization reaction (through CIs) and other non-radiative deactivation paths can be considered. It is worth noting that DCM is expected to have both locally excited and internal charge-transfer states in solution, at the origin of its well-known solvatochromism in emission. In the present CIs determination *in vacuo*, the solvent could not be taken into account and consequently, the role of the internal charge transfer state could not be properly modeled. The solvent effect is beyond the scope of our computational investigation.

Conclusions

The photoisomerization of a DCM analog (DCM-azide) was investigated experimentally and theoretically, shining light on its $E \leftrightarrow Z$ isomerization, which was demonstrated previously.[14] The relationships between the four isomers and conformers of DCM-azide were clarified by both experimental evidences (X-ray structures and spectroscopic data) as well as a full set of theoretical calculations (geometries, energies, electronic transitions, isomerization and interconversion pattern) *in vacuo* or including the solvent medium.

The fluorescence decay experiments confirmed that only the *E*-forms of DCM-azide are emissive. The emissive species in the fluorescence decay experiments were assigned to the *s-trans*-(*E*) (longer decay-time) and *s-cis*-(*E*) (shorter decay-time) forms of DCM-azide. The DFT/TDDFT and SF-TDDFT calculations of the four isomers and conformers provided a general pattern of the isomerization and interconversion paths in the ground and the excited states. Two conical intersections were identified, explaining the relaxation from the lowest excited state to the ground state, at the origin of the $E \leftrightarrow Z$ photoisomerization. They obviously play a great role in the competition between the fluorescence relaxation and the $E \leftrightarrow Z$ photoreaction, but also the *s-trans*↔*s-cis* conformational interconversion.

Experimental section and methods

Materials

All solvents used for steady-state spectroscopies were performed in spectroscopic pure grade reagents from Carlo Erba Reagents. The DCM-azide compound was prepared according to literature procedures.[30,36,37]

Steady-state absorption and emission spectroscopy

Steady-state spectroscopic absorption measurements were carried out with Agilent Technologies Cary 4000 and Cary 5000 spectrophotometers. The emission spectra were recorded with a Horiba Jobin-Yvon Fluorolog FL3-221 fluorescence spectrometer. The fluorescence quantum yield was determined by using Coumarin 153 in ethanol (ϕ_{em} = 0.544[38]) as a standard reference from Sigma-Aldrich.

Time-resolved fluorescence spectroscopy

Fluorescence decay curves were obtained by the time-correlated single-photon counting (TCSPC) method. The setup is composed of a titanium sapphire Ti:Sa oscillator (Spectra Physics, Maï Taï) emitting pulses of 100 fs duration for the fundamental laser beam, at a 80MHz frequency. The laser pulses then pass through a pulse picker which implements an acousto-optic modulator to reduce the repetition rate down to 4MHz. Non-linear SHG/THG crystals generate the desired wavelength (GWU Lasertechnik, UHG-23-PSK), then the beam is directed to the sample solution after adjusting the excitation power with an intensity attenuator filter wheel. Fluorescence photons are detected at 90° through a polarizer at the magic angle and a monochromator, by means of a micro-channels plate photomultiplier (MCP-PMT R3809U-50, Hamamatsu), connected to a TCSPC module (SPC-630, Becker & Hickl). Time-correlated fluorescence decay data are finally processed and analysed with the help of a software which implements reconvolution analysis and the global nonlinear last-squares minimization method (Globals, Laboratory for Fluorescence Dynamics at the University of California, Irvine).

X-ray crystallographic analysis

X-ray crystallographic analysis was carried out on the DCM-azide crystals. The isolated crystals were dried under vacuum at room temperature and shielded from the ambient light. X-ray diffraction was carried out using Rigaku XtaLabPro diffractometer equipped with a Mo microfocus sealed tube generator coupled to a double-bounce Max-Flux® multilayer optic and a HPAD PILATUS3 R 200K detector. Data collections were carried out using the software CrysAlisPro 1.171.41.96a.[39] SCALE3 ABSPACK scaling algorithm implemented within CrysAlisPro was applied to the processed data for the empirical absorption correction using spherical harmonics. The two structures were readily solved by intrinsic phasing methods (SHELXT program)[40] and refined by full-matrix least-squares methods on F^2 using SHELX-L.[41] Molecular graphics were prepared with ORTEP.[42]

Computational details

All the DFT and TDDFT calculations were performed by the Gaussian 16 software package.[43] The Pople 6-311++G(d,p), 6-311+G(d,p) and 6-31G(d) basis sets were adopted and the solvent effects were implemented with integral equation formalism of the polarizable continuum model (IEFPCM). The S_0 geometries of the four isomers and conformers were optimized at the PBE0/6-311++G(d,p) level. Regarding the computational cost, reduced size def2-SVP and 6-31G(d) basis sets were used for the excited states explorations and corresponding comparisons. The comparison of functionals and the basis set dependencies are shown in the ESI. From all optimized geometries, the vertical excitation energies and emission energies were calculated by the TDDFT method. The linear response (LR) method was implemented in the TDDFT calculations. The minimum energy CI calculations of S_0/S_1 in the $E \leftrightarrow Z$ isomerization process were located by the SF-TDDFT with the penalty-constrained (PC) optimization algorithm.[33,34,44,45] The SF-TDDFT/PC CI localizations were carried out at the PBE0/6-31G(d) level in gas phase by GAMESS-US (version 30 SEP 2020 (R2)).[46] All visualizations were implemented by GaussView 6 and VMD 1.9.3.[47,48]

Conflicts of interest

There are no conflicts to declare.

Author contributions

Conceptualization: R.M., F.M., S.M. (equal), J.X. (supporting); Data curation: Y.Z., P.R. (equal); Formal analysis: Y.Z. (lead), P.R., F.M. (supporting); Funding acquisition: R.M.; Investigation: Y.Z. (lead), P.R., R.M., F.M., L.C. (supporting); Methodology: Y.Z. (lead), R.M., F.M., S.M., P.R. (supporting); Project administration: R.M. (lead), F.M., S.M., J.X. (supporting); Resources: R.M., J.X., S.M., A.B. (equal); Software: Y.Z.; Supervision: R.M., F.M. (equal); Validation: Y.Z., R.M., F.M. (equal), S.M. (supporting); Visualization: Y.Z., R.M. (equal); Writing - original draft: Y.Z., R.M. (equal), P.R. (supporting); Writing - review & editing: Y.Z., R.M. (equal), F.M., L.C. (supporting).

Acknowledgements

The authors acknowledge Arnaud Brosseau for his kind help and support during the time-resolved fluorescence measurements. This work was performed by using HPC resources from the "Mésocentre" computing center of Centrale-Supélec and the École Normale Supérieure Paris-Saclay supported by the CNRS and the Région Ile-de-France (`http://mesocentre.centralesupelec.fr/`). Funding from the Agence Nationale de la Recherche (ANR-17-CE07-0056-01) is acknowledged.

Notes and references

1 D. Bléger and S. Hecht, *Angew. Chem. Int. Ed.*, 2015, **54**, 11338–11349.

2 M. Baroncini, M. Canton, L. Casimiro, S. Corra, J. Groppi, M. La Rosa, S. Silvi and A. Credi, *Eur. J. Inorg. Chem.*, 2018, **2018**, 4589–4603.

3 D. Roke, S. J. Wezenberg and B. L. Feringa, *Proc. Nat. acad. Sci.*, 2018, **115**, 9423–9431.

4 C. T. Kornman, L. Li, A. O. Weldeab, I. Ghiviriga, K. A. Abboud and R. K. Castellano, *Chem. Sci.*, 2020, **11**, 10190–10197.

5 M. Baroncini, S. d'Agostino, G. Bergamini, P. Ceroni, A. Comotti, P. Sozzani, I. Bassanetti, F. Grepioni, T. M. Hernandez, S. Silvi, M. Venturi and A. Credi, *Nat. Chem.*, 2015, **7**, 634–640.

6 F. Castiglioni, W. Danowski, J. Perego, F. K.-C. Leung, P. Sozzani, S. Bracco, S. J. Wezenberg, A. Comotti and B. L. Feringa, *Nat. Chem.*, 2020, **12**, 595–602.

7 S. L. Oscurato, M. Salvatore, P. Maddalena and A. Ambrosio, *Nanophotonics*, 2018, **7**, 1387–1422.

8 G. Das, T. Prakasam, M. A. Addicoat, S. K. Sharma, F. Ravaux, R. Mathew, M. Baias, R. Jagannathan, M. A. Olson and A. Trabolsi, *J. Am. Chem. Soc.*, 2019, **141**, 19078–19087.

9 K. Müller, A. Knebel, F. Zhao, D. Bléger, J. Caro and L. Heinke, *Chem. Eur. J.*, 2017, **23**, 5434–5438.

10 P. M. Toro, D. H. Jara, A. H. Klahn, D. Villaman,

M. Fuentealba, A. Vega and N. Pizarro, *Photochem. Photobiol.*, 2021, **97**, 61–70.
11 W. A. de Oliveira, D. Z. Mezalira and E. Westphal, *Liq. Cryst.*, 2021, **48**, 88–99.
12 B. Bai, M. Zhang, N. Ji, J. Wei, H. Wang and M. Li, *Chem. Commun.*, 2017, **53**, 2693–2696.
13 H. Karimi-Alavijeh, F. Panahi and A. Gharavi, *J. Appl. Phys.*, 2014, **115**, 093706.
14 L. Casimiro, S. Maisonneuve, P. Retailleau, S. Silvi, J. Xie and R. Métivier, *Chem. Eur. J.*, 2020, **26**, 14341–14350.
15 P. Hammond, *Opt. Commun.*, 1979, **29**, 331–333.
16 E. Marason, *Opt. Commun.*, 1981, **37**, 56–58.
17 J.-C. Mialocq and M. Meyer, *Laser Chem.*, 1990, **10**, 067392.
18 M.-k. Leung, C.-C. Chang, M.-H. Wu, K.-H. Chuang, J.-H. Lee, S.-J. Shieh, S.-C. Lin and C.-F. Chiu, *Org. Lett.*, 2006, **8**, 2623–2626.
19 Y.-S. Yao, J. Xiao, X.-S. Wang, Z.-B. Deng and B.-W. Zhang, *Adv. Funct. Mater.*, 2006, **16**, 709–718.
20 H. J. Yun, D. Y. Jung, D. K. Lee, A. K.-Y. Jen and J. H. Kim, *Dyes Pigm.*, 2015, **113**, 675–681.
21 J. Y. Kim, S. S. Yoon and Y. S. Kim13, *J. Nanosci. Nanotechnol.*, 2013, **13**, 1–4.
22 Z. Guo, W. Zhu and H. Tian, *Chem. Commun.*, 2012, **48**, 6073–6084.
23 M. Meyer, J. C. Mialocq and B. Perly, *J. Phys. Chem.*, 1990, **94**, 98–104.
24 M. Lesiecki, F. Asmar, J. Drake and D. M. Camaioni, *J. Lumin.*, 1984, **31**, 546–548.
25 J. Drake, M. L. Lesiecki and D. M. Camaioni, *Chem. Phys. Lett.*, 1985, **113**, 530–534.
26 M. Meyer, J. Mialocq and M. Rougee, *Chem. Phys. Lett.*, 1988, **150**, 484–490.
27 W. Rettig and W. Majenz, *Chem. Phys. Lett.*, 1989, **154**, 335–341.
28 J. Mialocq, X. Armand and S. Marguet, *Journal of Photochemistry and Photobiology A: Chemistry*, 1993, **69**, 351–356.
29 X. Xu, R. Zhang, Z. Cao and Q. Zhang, *J. Theor. Comput. Chem.*, 2008, **7**, 719–736.
30 K. Ouhenia-Ouadahi, R. Métivier, S. Maisonneuve, A. Jacquart, J. Xie, A. Léaustic, P. Yu and K. Nakatani, *Photochem. Photobiol. Sci.*, 2012, **11**, 1705–1714.
31 Y. Shao, M. Head-Gordon and A. I. Krylov, *J. Chem. Phys.*, 2003, **118**, 4807–4818.
32 F. Wang and T. Ziegler, *J. Phys. Chem.*, 2004, **121**, 12191–12196.
33 N. Minezawa and M. S. Gordon, *J. Phys. Chem. A*, 2009, **113**, 12749–12753.
34 N. Minezawa and M. S. Gordon, *J. Phys. Chem. A*, 2011, **115**, 7901–7911.
35 M. Winslow, W. B. Cross and D. Robinson, *J. Chem. Theory Comput.*, 2020, **16**, 3253–3263.
36 S. Maisonneuve, R. Métivier, P. Yu, K. Nakatani and J. Xie, *Beilstein J. Org. Chem.*, 2014, **10**, 1471–1481.
37 Y. Yu, N. Bogliotti, S. Maisonneuve, J. Tang and J. Xie, *Tetrahedron Lett.*, 2013, **54**, 1877–1883.
38 K. Rurack and M. Spieles, *Anal. Chem.*, 2011, **83**, 1232–1242.
39 Rigaku OD, *CrysAlis PRO*, 2015, Rigaku Oxford Diffraction, Yarnton, Oxfordshire, England.
40 Sheldrick, G. M., *Acta Crystallogr. A*, 2015, **71**, 3–8.
41 Sheldrick, G. M., *Acta Crystallogr. C*, 2015, **71**, 3–8.
42 M. N. Burnett and C. K. Johnson, *ORTEP-III*, 1996, ORNL-6895, Oak Ridge National Laboratory, Tennessee, USA.
43 M. J. Frisch, G. W. Trucks, H. B. Schlegel, G. E. Scuseria, M. A. Robb, J. R. Cheeseman, G. Scalmani, V. Barone, G. A. Petersson, H. Nakatsuji, X. Li, M. Caricato, A. V. Marenich, J. Bloino, B. G. Janesko, R. Gomperts, B. Mennucci, H. P. Hratchian, J. V. Ortiz, A. F. Izmaylov, J. L. Sonnenberg, D. Williams-Young, F. Ding, F. Lipparini, F. Egidi, J. Goings, B. Peng, A. Petrone, T. Henderson, D. Ranasinghe, V. G. Zakrzewski, J. Gao, N. Rega, G. Zheng, W. Liang, M. Hada, M. Ehara, K. Toyota, R. Fukuda, J. Hasegawa, M. Ishida, T. Nakajima, Y. Honda, O. Kitao, H. Nakai, T. Vreven, K. Throssell, J. A. Montgomery, Jr., J. E. Peralta, F. Ogliaro, M. J. Bearpark, J. J. Heyd, E. N. Brothers, K. N. Kudin, V. N. Staroverov, T. A. Keith, R. Kobayashi, J. Normand, K. Raghavachari, A. P. Rendell, J. C. Burant, S. S. Iyengar, J. Tomasi, M. Cossi, J. M. Millam, M. Klene, C. Adamo, R. Cammi, J. W. Ochterski, R. L. Martin, K. Morokuma, O. Farkas, J. B. Foresman and D. J. Fox, *Gaussian 16 Revision C.01*, 2016, Gaussian Inc. Wallingford CT.
44 B. G. Levine, C. Ko, J. Quenneville and T. J. MartÍnez, *Mol. Phys.*, 2006, **104**, 1039–1051.
45 B. G. Levine, J. D. Coe and T. J. Martínez, *J. Phys. Chem. B*, 2008, **112**, 405–413.
46 G. M. J. Barca, C. Bertoni, L. Carrington, D. Datta, N. De Silva, J. E. Deustua, D. G. Fedorov, J. R. Gour, A. O. Gunina, E. Guidez, T. Harville, S. Irle, J. Ivanic, K. Kowalski, S. S. Leang, H. Li, W. Li, J. J. Lutz, I. Magoulas, J. Mato, V. Mironov, H. Nakata, B. Q. Pham, P. Piecuch, D. Poole, S. R. Pruitt, A. P. Rendell, L. B. Roskop, K. Ruedenberg, T. Sattasathuchana, M. W. Schmidt, J. Shen, L. Slipchenko, M. Sosonkina, V. Sundriyal, A. Tiwari, J. L. Galvez Vallejo, B. Westheimer, M. Wloch, P. Xu, F. Zahariev and M. S. Gordon, *The Journal of Chemical Physics*, 2020, **152**, 154102.
47 R. Dennington, T. A. Keith and J. M. Millam, *GaussView Version 6*, 2019, Semichem Inc. Shawnee Mission KS.
48 W. Humphrey, A. Dalke and K. Schulten, *J. Mol. Graph. Model.*, 1996, **14**, 33–38.